

A SUBMILLIMETER CONTINUUM SURVEY OF LOCAL DUST-OBSCURED GALAXIES

JONG CHUL LEE¹, HO SEONG HWANG², AND GWANG-HO LEE³

¹ Korea Astronomy and Space Science Institute, 776 Daedeokdae-ro, Yuseong-gu, Daejeon 34055, Republic of Korea; jclee@kasi.re.kr

² School of Physics, Korea Institute for Advanced Study, 85 Hoegiro, Dongdaemun-gu, Seoul 02455, Republic of Korea

³ Department of Physics and Astronomy, Seoul National University, 1 Gwanak-ro, Gwanak-gu, Seoul 151-742, Republic of Korea

Last updated: May 14, 2018

ABSTRACT

We conduct a 350 μm dust continuum emission survey of 17 dust-obscured galaxies (DOGs) at $z = 0.05\text{--}0.08$ with the Caltech Submillimeter Observatory (CSO). We detect 14 DOGs with $S_{350\mu\text{m}} = 114\text{--}650$ mJy and $S/N > 3$. By including two additional DOGs with submillimeter data in the literature, we are able to study dust contents for a sample of 16 local DOGs that consists of 12 bump and 4 power-law types. We determine their physical parameters with a two-component modified blackbody function model. The derived dust temperatures are in the range 57–122 K and 22–35 K for the warm and cold dust components, respectively. The total dust mass and the mass fraction of warm dust component are $3\text{--}34 \times 10^7 M_{\odot}$ and 0.03–2.52%, respectively. We compare these results with those of other submillimeter-detected infrared luminous galaxies. The bump DOGs, the majority of the DOG sample, show similar distributions of dust temperatures and total dust mass to the comparison sample. The power-law DOGs show a hint of smaller dust masses than other samples, but need to be tested with a larger sample. These findings support that the reason why DOGs show heavy dust obscuration is not an overall amount of dust content, but probably the spatial distribution of dust therein.

Subject headings: galaxies: active – galaxies: evolution – galaxies: formation – galaxies: starburst – infrared: galaxies – submillimeter: galaxies

1. INTRODUCTION

The cosmic star formation rate density peaks at $z \sim 2$ and nearly half of the stars in present-day galaxies formed around this epoch (e.g., Dickinson et al. 2003; Magnelli et al. 2013; Behroozi et al. 2013). Understanding what drives this intense star formation is one of key issues in the study of cosmic star formation history (see Madau & Dickinson 2014 for a review). It is thus important to efficiently identify $z \sim 2$ star-forming galaxies to study the physical mechanisms responsible for the intense star formation activity. Interestingly, many star-forming galaxies in the distant Universe are infrared- and submillimeter-bright because a significant fraction of ultraviolet (UV) photons from young massive stars are absorbed by dust and then re-radiated in the infrared and submillimeter wavelengths (see Sanders & Mirabel 1996; Kennicutt 1998; Casey et al. 2014).

Among various methods to select high-redshift dusty star-forming galaxies, an optical-to-mid-infrared color cut $R - [24] \geq 14$ (mag in Vega, corresponding to $S_{24\mu\text{m}}/S_{0.65\mu\text{m}} \geq 982$) with a mid-infrared flux density cut $S_{24\mu\text{m}} \geq 0.3$ mJy (Dey et al. 2008; see also Houck et al. 2005; Fiore et al. 2008; Hwang et al. 2012; Rigucciniet al. 2015) has been widely used because of its simplicity. The galaxies satisfying this simple criterion are referred to as dust-obscured galaxies (DOGs); they experience heavy dust obscuration as the name suggests (e.g., Brand et al. 2007; Melbourne et al. 2011; Penner et al. 2012) and contribute to about 30% of the total infrared output in the Universe at $z \sim 2$ (e.g., Rigucciniet al. 2011; Calanog et al. 2013). Numerical simulations suggest that luminous DOGs result from extremely gas-rich galaxy mergers, while less luminous ones

are driven either by mergers or by secular evolution of gas-rich disk galaxies (Narayanan et al. 2010).

The DOGs are divided into two categories based on their spectral energy distribution (SED) shape at rest-frame near- and mid-infrared wavelengths: “bump” and “power-law” DOGs (Dey et al. 2008). The bump DOGs show a stellar photospheric bump at 1.6 μm (John 1988; Farrah et al. 2008), whereas the power-law DOGs show a monotonically increasing continuum attributed to hot dust component, indicating the presence of active galactic nuclei (AGNs; Houck et al. 2005; Desai et al. 2009; but see also Narayanan et al. 2010). In the merger-driven scenario of DOG formation, the DOGs are thought to evolve from bump (i.e., starburst-dominated) to power-law (AGN-dominated) types (e.g., Narayanan et al. 2010; Bussmann et al. 2011). Some very luminous DOGs ($L_{\text{IR}} \gtrsim 10^{13} L_{\odot}$) appear as so-called hot DOGs, which are mainly powered by deeply buried AGNs (see Wu et al. 2012; Jones et al. 2014; Assef et al. 2015; Toba & Nagao 2016). Therefore, studying the DOGs can provide important hints of a possible evolutionary link among high- z galaxies and the connection between star formation and nuclear activity. However, because of their extreme distances, it is difficult to compare the observational features with model predictions, which is crucial for understanding what makes a DOG have such large dust obscuration.

To study the physical properties of DOGs in detail Hwang & Geller (2013, hereafter HG13) focused on local analogs of these galaxies that have a wealth of multiwavelength data available (see also Heckman et al. 2005; Juneau et al. 2014; Greis et al. 2016; Bian et al. 2016). Using the multiwavelength data from UV to far-infrared that include *Galaxy Evolution Explorer*

(*GALEX*; Martin et al. 2005), Sloan Digital Sky Survey (SDSS; York et al. 2000) data release 7 (DR7; Abazajian et al. 2009), *Wide-field Infrared Survey Explorer* (*WISE*; Wright et al. 2010), *Infrared Astronomical Satellite* (*IRAS*; Neugebauer et al. 1984), and *AKARI* Space Telescope (Murakami et al. 2007), HG13 identified 47 DOGs at $0.05 < z < 0.08$ with extreme flux density ratios between mid-infrared (*WISE* $12\ \mu\text{m}$) and near-UV (*GALEX* $0.22\ \mu\text{m}$) bands (i.e., $S_{12\mu\text{m}}/S_{0.22\mu\text{m}} \geq 892$). Comparison of local DOGs to other galaxies with lower $S_{12\mu\text{m}}/S_{0.22\mu\text{m}}$ shows that local DOGs have a relatively large Balmer decrement ($H\alpha/H\beta$), small optical size, and large elongation. On the other hand, there are no significant differences in specific star formation rate and in large- and small-scale environments between the two sample.

The multiwavelength data for the DOGs in HG13 mainly cover only $\lambda \leq 100\ \mu\text{m}$; there are few data on the ‘Rayleigh-Jeans’ side of the infrared SED peak, which is important to quantify dust properties of galaxies accurately (Hwang et al. 2010b; Dale et al. 2012; Symeonidis et al. 2013). Therefore, Hwang et al. (2013, hereafter HAG13) conducted Submillimeter Array (SMA) observations of four local DOGs to probe $880\ \mu\text{m}$ continuum emissions. They derived dust temperatures and masses using a two-component dust model (warm and cold dust components associated with stellar birth clouds and diffuse interstellar medium, respectively; see Charlot & Fall 2000; Dunne & Eales 2001; Sauvage et al. 2005; Vlahakis et al. 2005; da Cunha et al. 2008; Willmer et al. 2009) and found that the dust properties of local DOGs are similar to those of other infrared luminous galaxies with submillimeter detection. HAG13 thus concluded that the DOGs are not a distinctive population among dusty galaxies; probably the reason why some galaxies appear as DOGs is not an extremely large dust content, but simply results from a large dust obscuration along the line of sight.

There were only four local DOGs with submillimeter detection in HAG13. To test further the idea on the nature of local DOGs using a larger sample with submillimeter detection, we extend the dust continuum emission survey of local DOGs with the 10.4 m single-dish antenna of the Caltech Submillimeter Observatory (CSO) in this study. The structure of this paper is as follows. We explain the target selection, CSO observations, and data reduction in Section 2. We derive physical parameters of dust content in the local DOGs and compare them with those of other submillimeter-detected galaxies in Section 3. We summarize and discuss the results in Section 4. Throughout this paper, we adopt the flat Λ CDM cosmological parameters: $H_0 = 70\ \text{km s}^{-1}\ \text{Mpc}^{-1}$, $\Omega_\Lambda = 0.7$, and $\Omega_m = 0.3$.

2. DATA

2.1. Targets

HG13 identified 47 local DOGs satisfying the criteria of $S_{12\mu\text{m}}/S_{0.22\mu\text{m}} \geq 892$, $S_{12\mu\text{m}} > 20\ \text{mJy}$, and $0.05 < z < 0.08$. We first fitted to their multiwavelength data at $\lambda > 6\ \mu\text{m}$ with the SED templates and fitting routine of DECOMPIR¹ (Mullaney et al. 2011) to predict $350\ \mu\text{m}$ flux densities. We then selected 26 bright local DOGs

with the expected $350\ \mu\text{m}$ flux densities $\geq 100\ \text{mJy}$ and with R.A. = 9–18 hours that could be observable in 2014 March and April runs.

2.2. Observations and Data Reduction

Among the 26 targets, 17 objects were actually observed with the CSO telescope over four nights under moderate weather conditions (the opacity at 225 GHz $\tau_{225} = 0.04\text{--}0.10$). The total integration time for each object is 20–80 minutes by excluding bad scans. We also observed Ganymede and Callisto for pointing, focusing, and flux calibration at the beginning and middle of each night (i.e., once every three or four hours). The pointing accuracy is $\sim 4''$ rms and the flux density uncertainty introduced by the calibration error is typically 5–10%.

The observations were carried out with the second-generation Submillimeter High Angular Resolution Camera (SHARC-II; Dowell et al. 2003) that has a bolometer array with 32×12 pixels. The field of view and beam size (FWHM) of SHARC-II at $350\ \mu\text{m}$ are $2'.6 \times 1'.0$ and $8''.5$, respectively. The CSO Dish Surface Optimization System (DSOS; Leong et al. 2006) was activated to minimize the surface imperfections and gravitational deformations. To map the area around compact sources including our targets and calibrators, the telescope was swept in the standard Lissajous pattern with amplitudes of $\pm 20''$ and $\pm 10''$ in azimuth and elevation, respectively, resulting in a uniform coverage of $115'' \times 38''$.

We reduced the data using the Comprehensive Reduction Utility for SHARC-II (CRUSH) software package² (Kovács 2006), version crush-2.20-3. The option ‘‘faint’’ in CRUSH was applied because targets were faint, but still visible in a single scan. The output map had a pixel scale of $1''.62\ \text{pixel}^{-1}$ and was smoothed to an effective FWHM of $12''.4$ for optimal detection. The photometry was conducted with a $20''$ diameter aperture, large enough to capture the instrumental flux density of each source. The sky level and photometric measurement error were calculated by computing the mean and rms within ~ 10 off-source apertures. We applied the same procedure to the calibrators and derived scaling factors that convert the instrumental flux density to a physical flux density. Among the 17 observed DOGs, 14 ones were detected with signal-to-noise (S/N) > 3 in the synthesis maps. The other three DOGs were not detected even though we used the option ‘‘deep’’ for very faint sources in the data reduction.

We list the CSO observation log of 17 DOGs in Table 1 with their $350\ \mu\text{m}$ flux densities or 3σ upper limits. The flux density uncertainties include the measurement and calibration errors. We found the *Herschel* $350\ \mu\text{m}$ photometric data for LDOG–07 ($609.9 \pm 8.1\ \text{mJy}$) from the *Herschel*-ATLAS program (Rigby et al. 2011), which agrees with our measurement ($475.9 \pm 86.0\ \text{mJy}$) within 1.6σ level. We display the CSO $350\ \mu\text{m}$ continuum images in Figure 1 with the optical color images from SDSS *gri*-band data. Although some DOGs appear extended in the CSO images, it is not easy to say that they are spatially resolved because the focus correction was not frequently made during observations.

3. RESULTS

¹ <http://sites.google.com/site/decompir>

² <http://www.submm.caltech.edu/~sharc/crush>

TABLE 1
CSO OBSERVATION LOG

ID	SDSS ObjID (DR9)	R.A. ₂₀₀₀	Decl. ₂₀₀₀	z	UT Date	τ_{225}	Int. (min)	S_{350} (mJy)
LDOG-07	1237674462024106294	09:04:01.02	+01:27:29.12	0.0534	2014 Mar 19	0.088	28.4	475.9±86.0
LDOG-09	1237663530802937978	09:38:19.17	+64:37:21.26	0.0710	2014 Mar 19	0.084	48.0	650.0±216.5
LDOG-14	1237654605860110514	10:17:31.29	+04:36:19.04	0.0572	2014 Apr 10	0.063	38.2	180.0±31.9
LDOG-22	123767114147777656	11:29:56.35	-06:24:20.48	0.0523	2014 Apr 7	0.054	19.1	538.2±146.7
LDOG-23	1237657611801657347	11:35:49.09	+56:57:08.27	0.0514	2014 Mar 19	0.065	76.2	257.3±85.7
LDOG-26	1237667209992732748	12:21:34.35	+28:49:00.12	0.0613	2014 Apr 7	0.102	57.2	312.8±83.2
LDOG-27	1237667736660017246	12:56:25.47	+23:20:55.05	0.0742	2014 Apr 8	0.056	37.9	327.5±48.1
LDOG-28	1237665129084092587	12:56:42.72	+35:07:29.92	0.0547	2014 Apr 8	0.043	38.0	210.4±32.9
LDOG-33	1237665430241149030	13:41:02.95	+29:36:42.86	0.0773	2014 Apr 10	0.061	47.3	220.4±33.7
LDOG-39	1237648705135051235	15:26:37.67	+00:35:33.50	0.0507	2014 Apr 10	0.057	76.4	114.1±22.3
LDOG-41	1237662663216070833	15:51:53.04	+27:14:33.65	0.0589	2014 Apr 10	0.070	16.4	345.9±43.3
LDOG-44	1237661387621073252	16:53:37.16	+30:26:09.76	0.0732	2014 Apr 8	0.058	37.9	341.1±31.2
LDOG-45	1237668681527132368	17:03:30.38	+45:40:47.15	0.0604	2014 Apr 10	0.049	48.0	157.0±28.1
LDOG-46	1237656530531254308	17:38:01.52	+56:13:25.81	0.0652	2014 Apr 10	0.095	47.6	131.4±27.0
LDOG-13	1237661383848951984	10:11:01.09	+38:15:19.74	0.0527	2014 Apr 8	0.066	76.1	<91.3
LDOG-16	1237648722831868077	10:33:33.15	+01:06:35.15	0.0657	2014 Apr 10	0.060	57.3	<203.3
LDOG-19	1237651067886502124	11:02:13.01	+64:59:24.86	0.0776	2014 Mar 19	0.064	84.4	<200.2

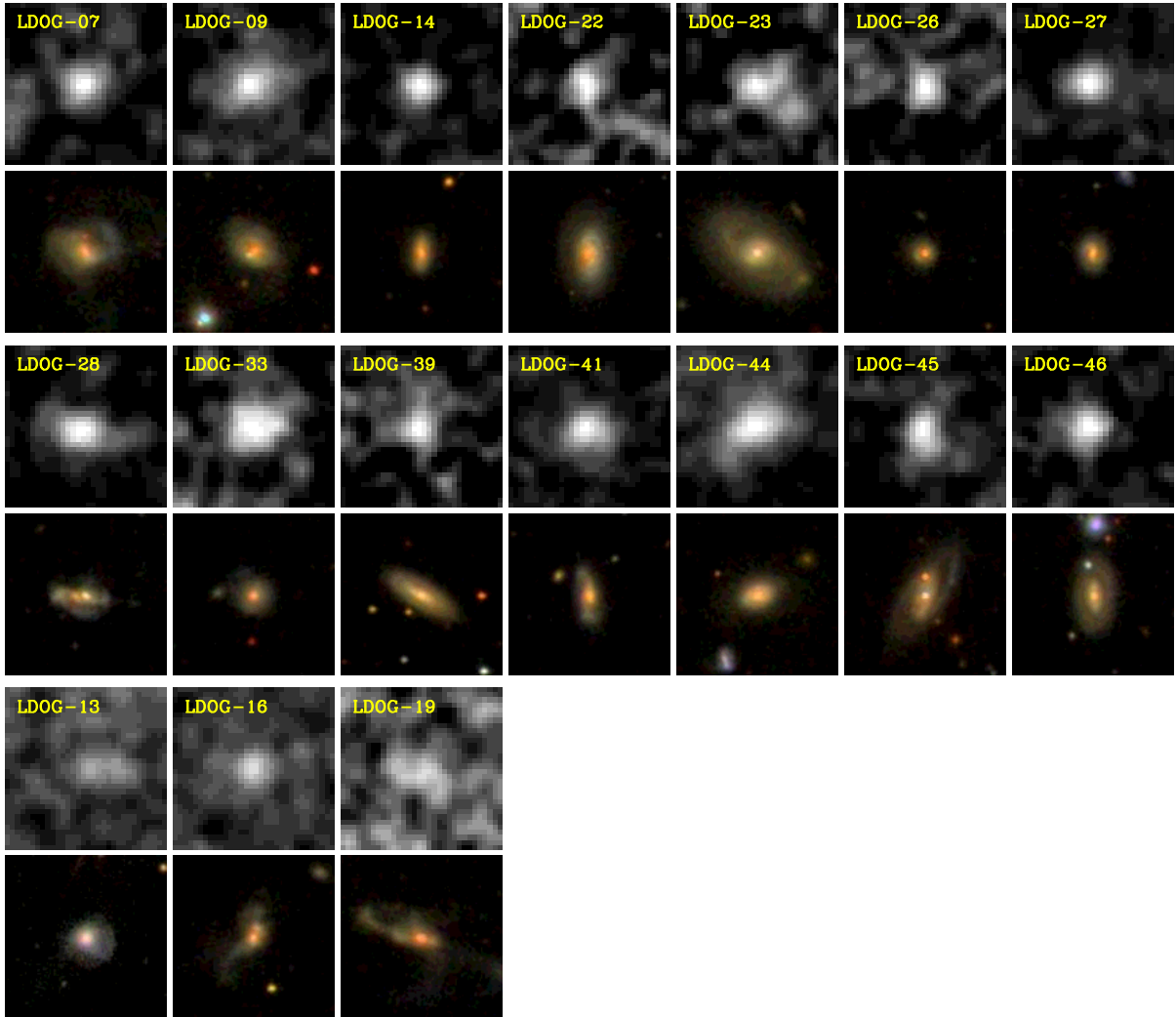


FIG. 1.— CSO synthesis maps of the 350 μm continuum emission (1st, 3rd, and 5th rows) and SDSS cut-out images (RGB color composites from *irg* bands; 2nd, 4th, and 6th rows) for the 17 CSO-observed DOGs. The size of each image is $48'' \times 48''$ (55.6 kpc at $\langle z \rangle = 0.06$). North is up and east is to the left.

3.1. Deriving Dust Temperatures and Masses of Local DOGs

We derive the physical parameters of dust content of the 14 local DOGs by fitting to the multiwavelength data including our 350 μm submillimeter observations. We again adopt the SED fitting routine of DECOMPIR to derive the total (8–1000 μm) infrared luminosities and to decompose the infrared SEDs into AGN and host-galaxy components. The DECOMPIR routine contains the SED templates consisting of one AGN SED and five groups of host-galaxy SEDs. These templates are produced from the spectroscopic data of *Spitzer* infrared spectrograph and the photometric data of *IRAS* for AGN-host and starburst galaxies (see [Mullaney et al. 2011](#) for more details). We fit to the data at $\lambda > 6 \mu\text{m}$ with these SED templates, and choose the best-fit template that provides the lowest χ^2 value for each galaxy. The left panels of Figure 2 show the photometric data of the 14 local DOGs with CSO 350 μm detection and their best-fit SEDs from DECOMPIR. We do not use the SMA 880 μm upper limit flux densities of LDOG–39 and LDOG–41 for the SED fits as HAG13 did. The total infrared luminosities are in the range $1.60 \times 10^{11} \leq L_{\text{IR}}/L_{\odot} \leq 5.43 \times 10^{11}$. The AGN contribution to the infrared luminosity varies 0.0% to 44.4%.

We then derive the dust temperatures and masses by fitting to the infrared and submillimeter data at $\lambda > 20 \mu\text{m}$ with a two-component modified blackbody model. For the optically thin case, this model has the form in the rest-frame:

$$S_{\nu} = A_w \nu^{\beta} B_{\nu}(T_{\text{warm}}) + A_c \nu^{\beta} B_{\nu}(T_{\text{cold}}), \quad (1)$$

where T_{warm} and T_{cold} are the dust temperatures of warm and cold components, respectively. A_w and A_c are the relative contributions of the two components, $B_{\nu}(T)$ is the Planck function, and β is the dust emissivity index. The dust emissivity index β can vary between 1 and 2 depending on several dust parameters (e.g., dust grain size, composition, temperature; [Draine & Lee 1984](#); [Rémy-Ruyer et al. 2013](#)), but it is usually fixed for the fit when the number of data points is small (e.g., $\beta = 1.5$: [Boselli et al. 2012](#); [Rigucciniet al. 2015](#); $\beta = 2.0$: [Willmer et al. 2009](#); [Cortese et al. 2012](#)). We test two cases with $\beta = 1.5$ and 2.0, and adopt $\beta = 2.0$ that provides better fits for our sample.

Then the dust mass can be derived by ([Hildebrand 1983](#))

$$M_{\text{dust}} = M_{\text{warm}} + M_{\text{cold}} = \frac{D_L^2 \nu^{\beta}}{k_{\nu}} (A_w + A_c), \quad (2)$$

where D_L is the luminosity distance and k_{ν} is the dust mass opacity coefficient (absorption cross section per unit dust mass). To be consistent with HAG13, we adopt k_{ν} at 850 μm (k_{850}) = 0.383 $\text{cm}^2 \text{g}^{-1}$ from [Draine \(2003\)](#). This dust mass opacity coefficient k_{ν} can be very uncertain, thus the resulting dust mass can change by a factor of two (e.g., $k_{850} = 0.77 \text{cm}^2 \text{g}^{-1}$ in [James et al. 2002](#)). Comparison of dust masses with other studies should be carefully made by considering different k_{ν} . The right panels of Figure 2 show the best-fit SEDs from the two-component modified blackbody function model. Again, we do not use the SMA 880 μm upper limit flux densities of LDOG–39 and LDOG–41 for the SED fits.

In Table 2, we list the derived physical parameters including total infrared luminosity, AGN contribution to the infrared luminosity, dust temperatures of warm and cold components, total dust mass, and mass fraction of warm dust component. We determine the uncertainty for each parameter by generating 1000 SEDs within the associated photometric error (assumed to be Gaussian distribution) and then calculating the standard deviation of SED fitting results. It should be noted that these uncertainties could be underestimated, especially the total infrared luminosity and the AGN contribution. This is because the uncertainties may just reflect the uncertainty in the fitting procedure, not taking fully into account the discrepancy between the data and the best-fit model that could be due to the incompleteness of SED models at longer wavelengths and the difficulty in modeling the intrinsic AGN infrared SEDs. For the following analysis, we add two DOGs that are not observed in this study, but have submillimeter data in the archive: LDOG–08 and LDOG–35 (see HAG13 for details).

3.2. Comparison of Dust Properties between Local DOGs and Other Infrared Luminous Galaxies

To compare the dust properties of local DOGs with other infrared luminous galaxies, HAG13 constructed a comparison sample of galaxies with submillimeter detection in the literature. This sample contains 62 galaxies with SCUBA 850 μm data from the SCUBA local universe galaxy survey (SLUGS: [Dunne et al. 2000](#); [Dunne & Eales 2001](#)) and/or SMA 880 μm data from [Wilson et al. \(2008\)](#). Their mid- and far-infrared data are adopted from HG13 and from the Great Observatories All-sky LIRG Survey (GOALS: [Armus et al. 2009](#); [U et al. 2012](#)). The galaxies in the comparison sample do not satisfy the color criterion of DOGs. HAG13 also removed very nearby galaxies at $z \leq 0.01$ and interacting systems from the comparison sample (see HAG13 for more details).

There have been several submillimeter data available for local dusty star-forming galaxies since HAG13 (e.g., [Clemens et al. 2013](#); [Ciesla et al. 2014](#); [Clark et al. 2015](#)). However, we did not add these galaxies in the comparison sample because most of them have $L_{\text{IR}} \lesssim 10^{11} L_{\odot}$ that are different from the infrared luminosity range of local DOGs. Although we apply the same SED fitting method to both local DOGs and galaxies in the comparison sample (hereafter comparison galaxies), it is not always straightforward to compare them because of their inhomogeneous selection criteria. We therefore focus mainly on relative differences of several dust properties.

Figures 3 and 4 display several parameters related to the dust temperature and mass as a function of total infrared luminosity. The large circles and small squares denote the local DOGs and the comparison galaxies, respectively. Each symbol is color-coded according to the AGN contribution to infrared luminosity. Open histogram is for all the comparison galaxies regardless of their infrared luminosities. The red and blue histograms show the distributions for 16 local DOGs and 35 comparison galaxies in the same range of infrared luminosity ($1.19 \times 10^{11} \leq L_{\text{IR}}/L_{\odot} \leq 5.43 \times 10^{11}$). For fair comparison, we mainly discuss the difference between the red and blue histograms. We run the Kolmogorov-Smirnov (K-

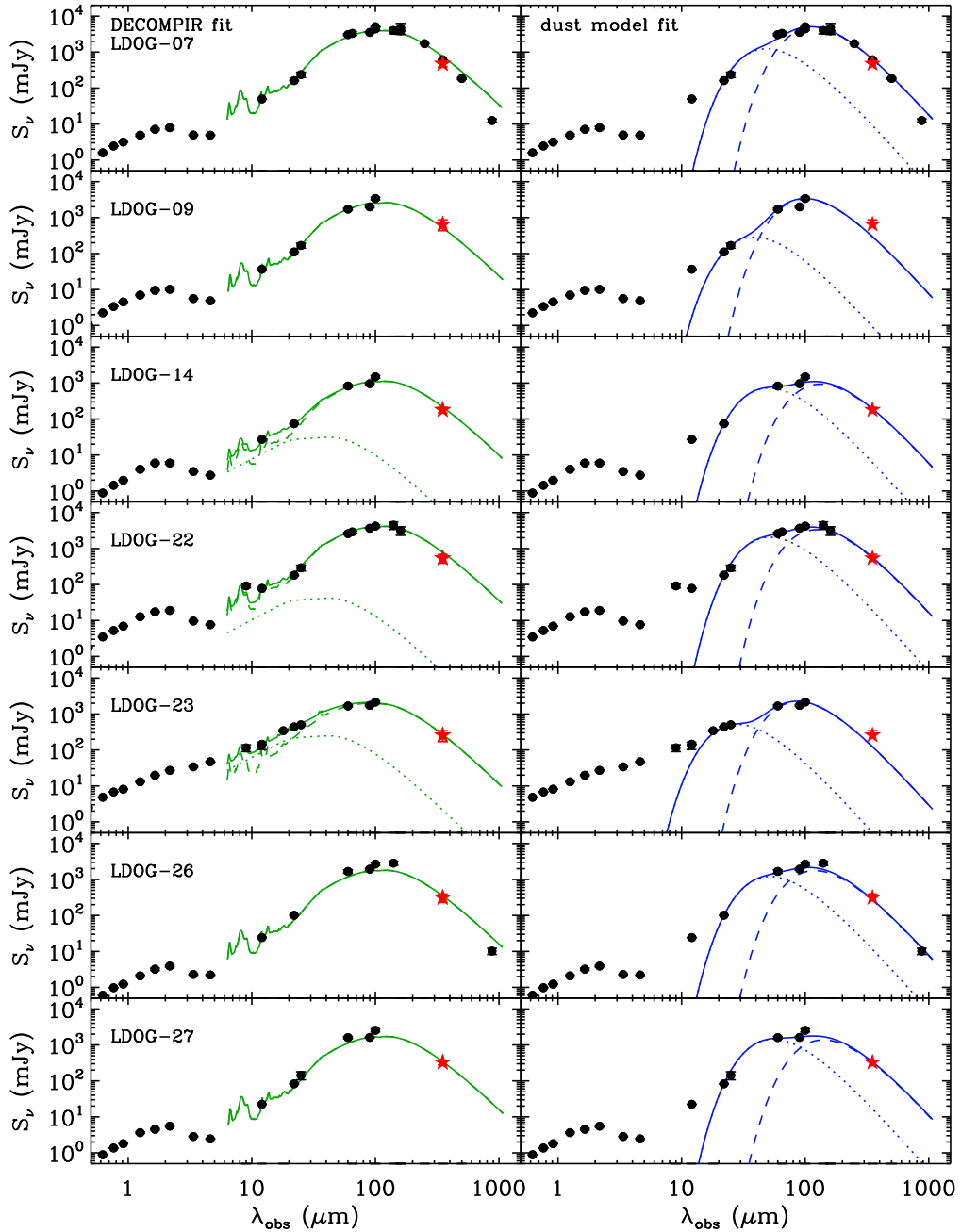


FIG. 2.— SEDs of the 14 DOGs with CSO detection. Black circles and downward arrows (for 3σ upper limits) are photometric data compiled in HG13 and HAG13, while red stars represent our $350\ \mu\text{m}$ observations. Error bars are shown for all the points but are mostly smaller than the symbols. In the left panels, green solid, dotted, and dashed lines indicate the best-fit SEDs with the DECOMPIR routine of Mullaney et al. (2011) for total, AGN and host-galaxy components, respectively. In the right panels, blue solid, dotted, and dashed lines represent the total, warm and cold dust components from the two-component modified blackbody function fits.

S) test and the Anderson-Darling (A-D) k-sample test on the distributions between the two samples, and list the relevant p-values³ in each figure.

The dust temperature and mass of local DOGs appear not to change with infrared luminosity, but the dynamic range for the infrared luminosity is very small (~ 0.7 dex). For the comparison galaxies, the cold dust temperature T_{cold} is well correlated with infrared luminos-

ity (Spearman’s rank correlation coefficient = 0.47 and the probability of obtaining the correlation by chance = 0.03%), while the warm dust temperature T_{warm} is not (see Dunne & Eales 2001). The total dust mass M_{dust} shows a good correlation with infrared luminosity (Spearman’s rank correlation coefficient = 0.50 and the probability of obtaining the correlation by chance < 0.01%), consistent with previous studies (e.g., Dunne & Eales 2001; Magdis et al. 2012). The dust-to-stellar mass⁴ ra-

³ The p-value is involved in the probability that two test samples are extracted from the same parent population. In general, a p-value < 0.05 is considered that the two distributions are significantly different.

⁴ The stellar masses are drawn from the MPA/JHU DR7 value-added galaxy catalogue (Kauffmann et al. 2003). Note that 19% and 69% of the local DOGs and the comparison galaxies do not

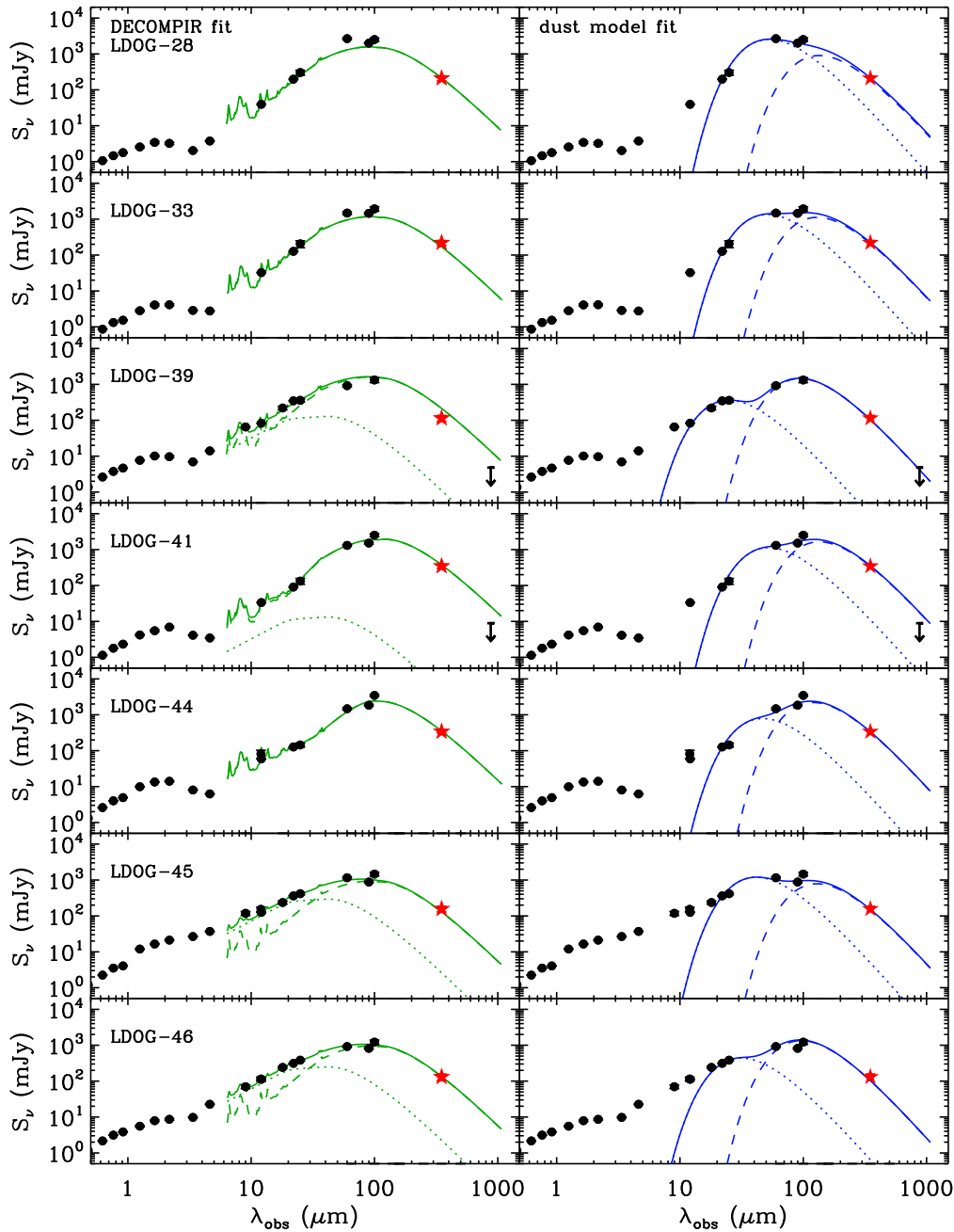


Fig. 2.— Continued

tio $M_{\text{dust}}/M_{\text{star}}$ and the mass fraction of warm dust component $M_{\text{warm}}/M_{\text{dust}}$ are weakly correlated with infrared luminosity.

In the top and middle panels of Figure 3, both local DOGs and comparison galaxies show that T_{cold} is in a narrow range 20–40 K, but T_{warm} is a wide range 46–122 K. The K-S and A-D k-sample tests cannot reject the null hypothesis that the dust temperature distributions between the two samples are drawn from the same parent population. The bottom panels display the flux density ratios of *IRAS* 25 to 60 μm , S_{25}/S_{60} , which is a model-independent warm dust temperature indicator

have the MPA masses because they are not in a spectroscopic sample of SDSS DR7.

(see Magdis et al. 2013). Two samples show no significantly different distributions. The S_{25}/S_{60} are closely related to the AGN contribution and the warm dust temperature in the sense that AGN-dominated galaxies usually have larger S_{25}/S_{60} (see green and blue symbols; de Grijp et al. 1985; Veilleux et al. 2009; Lee et al. 2012). For comparison, we also plot the *IRAS*-detected SDSS galaxies at $z > 0.01$ regardless of submillimeter detection (gray dots and contours; Hwang et al. 2010a). The S_{25}/S_{60} of both local DOGs and comparison galaxies are slightly smaller than those of *IRAS*-detected SDSS galaxies probably because the formers are relatively bright at long wavelengths (i.e., they are submillimeter-detected; see Magdis et al. 2010).

In the top panels of Figure 4, the dust masses of local

TABLE 2
SED FIT RESULTS

ID	L_{IR} ($\times 10^{11} L_{\odot}$)	f_{AGN} (%)	T_{warm} (K)	T_{cold} (K)	M_{dust} ($\times 10^8 M_{\odot}$)	$M_{\text{warm}}/M_{\text{dust}}$ ($\times 10^{-3}$)
LDOG-07	4.49 ^{+0.02} _{-0.02}	0.0 ^{+0.0} _{-0.0}	62.9 ^{+1.9} _{-1.2}	26.6 ^{+0.2} _{-0.2}	2.46 ^{+0.04} _{-0.04}	3.5 ^{+0.8} _{-0.8}
LDOG-09	5.43 ^{+0.07} _{-0.07}	0.0 ^{+0.0} _{-0.0}	80.1 ^{+21.} _{-9.2}	30.9 ^{+1.3} _{-2.1}	1.45 ^{+9.99} _{-0.33}	0.7 ^{+1.7} _{-0.4}
LDOG-14	1.60 ^{+0.04} _{-0.04}	8.2 ^{+0.7} _{-0.7}	60.7 ^{+1.5} _{-1.1}	23.1 ^{+12.} _{-0.9}	1.11 ^{+0.31} _{-0.48}	6.2 ^{+2.3} _{-2.8}
LDOG-22	4.63 ^{+0.05} _{-0.05}	3.1 ^{+0.3} _{-0.4}	58.9 ^{+15.} _{-1.0}	24.7 ^{+3.5} _{-1.1}	2.41 ^{+0.87} _{-0.89}	7.9 ^{+2.0} _{-2.6}
LDOG-23	3.48 ^{+0.11} _{-0.11}	23.9 ^{+1.9} _{-2.0}	108.1 ^{+15.} _{-8.6}	35.0 ^{+1.6} _{-1.5}	0.27 ^{+0.08} _{-0.06}	0.8 ^{+0.8} _{-0.4}
LDOG-26	2.74 ^{+0.31} _{-0.58}	0.0 ^{+0.0} _{-0.0}	59.1 ^{+4.8} _{-1.4}	25.7 ^{+9.5} _{-1.0}	1.44 ^{+0.27} _{-0.52}	10.5 ^{+3.9} _{-5.0}
LDOG-27	3.94 ^{+0.05} _{-0.05}	0.0 ^{+0.0} _{-0.0}	56.7 ^{+28.} _{-0.7}	22.2 ^{+3.0} _{-0.9}	3.42 ^{+0.78} _{-0.82}	9.6 ^{+2.9} _{-2.1}
LDOG-28	2.39 ^{+0.05} _{-0.03}	0.0 ^{+0.3} _{-0.0}	58.0 ^{+9.6} _{-0.6}	22.7 ^{+17.} _{-1.4}	1.10 ^{+0.35} _{-0.66}	25.2 ^{+7.9} _{-14.}
LDOG-33	3.76 ^{+0.05} _{-0.04}	0.0 ^{+0.0} _{-0.0}	61.0 ^{+2.1} _{-0.9}	24.1 ^{+8.6} _{-1.1}	2.03 ^{+0.51} _{-0.67}	11.3 ^{+3.6} _{-3.7}
LDOG-39	2.46 ^{+0.07} _{-0.07}	17.0 ^{+1.3} _{-1.4}	122.2 ^{+39.} _{-17.}	32.4 ^{+1.4} _{-1.3}	0.25 ^{+0.07} _{-0.06}	0.3 ^{+0.7} _{-0.2}
LDOG-41	2.76 ^{+0.08} _{-0.09}	2.1 ^{+0.6} _{-0.6}	58.5 ^{+0.8} _{-0.6}	22.8 ^{+0.9} _{-0.8}	2.24 ^{+0.46} _{-0.41}	6.1 ^{+1.5} _{-0.9}
LDOG-44	4.71 ^{+0.06} _{-0.06}	0.0 ^{+0.5} _{-0.0}	66.3 ^{+75.} _{-2.5}	26.0 ^{+2.4} _{-0.9}	2.43 ^{+0.44} _{-0.70}	3.3 ^{+1.5} _{-2.0}
LDOG-45	3.13 ^{+0.07} _{-0.07}	44.4 ^{+1.7} _{-1.7}	74.3 ^{+26.} _{-1.3}	23.8 ^{+11.} _{-1.2}	0.91 ^{+0.31} _{-0.50}	5.1 ^{+8.0} _{-1.7}
LDOG-46	3.51 ^{+0.09} _{-0.09}	39.8 ^{+2.1} _{-2.0}	98.4 ^{+5.8} _{-8.6}	32.1 ^{+1.5} _{-3.0}	0.40 ^{+0.12} _{-0.15}	1.2 ^{+9.9} _{-0.4}

DOGs seem to be on average larger than those of comparison galaxies. However when we plot the dust masses normalized by stellar masses ($M_{\text{dust}}/M_{\text{star}}$) in the middle panels, we do not see such a difference. The statistical tests also confirm that overall dust masses of local DOGs are indistinguishable from those of other infrared luminous galaxies. In the bottom panels, there is no significant difference in the mass fraction of warm dust component ($M_{\text{warm}}/M_{\text{dust}}$) between the two samples ($p_{\text{KS}} = 0.18$ and $p_{\text{AD}} = 0.19$). However, if we exclude the galaxies with a relatively large AGN contribution (i.e., $f_{\text{AGN}} > 10\%$, the warm dust parameters of these galaxies could be contaminated by AGNs), the difference between the two samples is significant ($p_{\text{KS}} = 0.02$ and $p_{\text{AD}} = 0.03$). Note that when the AGN-dominated galaxies are excluded, the p -values change dramatically only for the warm dust mass fraction.

4. DISCUSSION AND SUMMARY

We conducted CSO observations of 350 μm dust continuum emission for 17 local DOGs. By excluding three non-detected DOGs and by including two DOGs with submillimeter data from the literature, we derived their physical parameters of dust content from the SED fits with a two-component dust model. Comparisons between the local DOGs and other submillimeter-detected infrared luminous galaxies show no significant difference in cold and warm dust temperatures and in total dust mass.

The two-component dust model in this study is composed of two emissivity-modified blackbody functions, representing the warm and cold dust components. Although there are more sophisticated models that account for various dust parameters (e.g., [Draine & Li 2007](#); [da Cunha et al. 2008](#)), this two-component model is good enough to fit to the photometric data points at $\lambda > 20 \mu\text{m}$; this does not include the mid-infrared part where the contributions of polycyclic aromatic hydrocarbon (PAH) emission features and stochastic heating processes are important (see [Walcher et al. 2011](#) for a review). Actually, HAG13 show that dust masses derived from the two-component model agree well with those

from [Draine & Li \(2007\)](#) model (but see also [Berta et al. 2016](#)). [Kirkpatrick et al. \(2015\)](#) also conclude that the optically thin two-component modified blackbody model adopted in this study is a reasonable choice for determining dust parameters compared to other methods including optically thick dust, fixed dust temperatures, and single-/three-component model.

According to the definition of [Dey et al. \(2008\)](#), the 16 local DOGs in this study can be classified into 4 power-law and 12 bump types. Remarkably, all power-law DOGs have $f_{\text{AGN}} > 20\%$ and all bump DOGs have $f_{\text{AGN}} \leq 20\%$. In the comparison sample of 35 galaxies with infrared luminosities similar to DOGs, there is only one galaxy with $f_{\text{AGN}} > 20\%$. When we consider the AGN classification result of HG13 based on optical emission line ratio diagrams ([Baldwin et al. 1981](#); [Veilleux & Osterbrock 1987](#); [Kewley et al. 2006](#)), the number fractions of AGNs among local DOGs and other galaxies are $51.1 \pm 7.3\%$ and $21.3 \pm 3.4\%$, respectively. These confirm an important role of AGNs in local DOGs as an energy source, especially for power-law DOGs.

The SEDs of warm dust and AGN components overlap significantly in the mid-infrared wavelengths. Because we consider each component separately, dust parameters related to warm component could be strongly affected by the AGN contamination. For example, the galaxies with $f_{\text{AGN}} > 10\%$ are outliers in the plot of S_{25}/S_{60} vs. L_{IR} (bottom left panel of [Figure 3](#)), suggesting their warm dust parameters may not be reliable. There are several SED fitting codes that account for dust and AGN emission simultaneously (e.g., [Berta et al. 2013](#); [Ciesla et al. 2015](#)), but these codes are not useful to this study because we would like to split the dust emission heated by star formation into warm and cold components. The AGN contamination is significant only in the mid-infrared wavelengths (e.g., [Assef et al. 2010](#); [Lee et al. 2013](#)), but not in the far-infrared/submillimeter wavelengths (e.g., [Hatziminaoglou et al. 2010](#); [Lee et al. 2011](#); [Hwang et al. 2011](#); [Kirkpatrick et al. 2012](#)). Therefore, the cold dust related parameters are not affected much even in AGN-dominated galaxies. The total dust mass

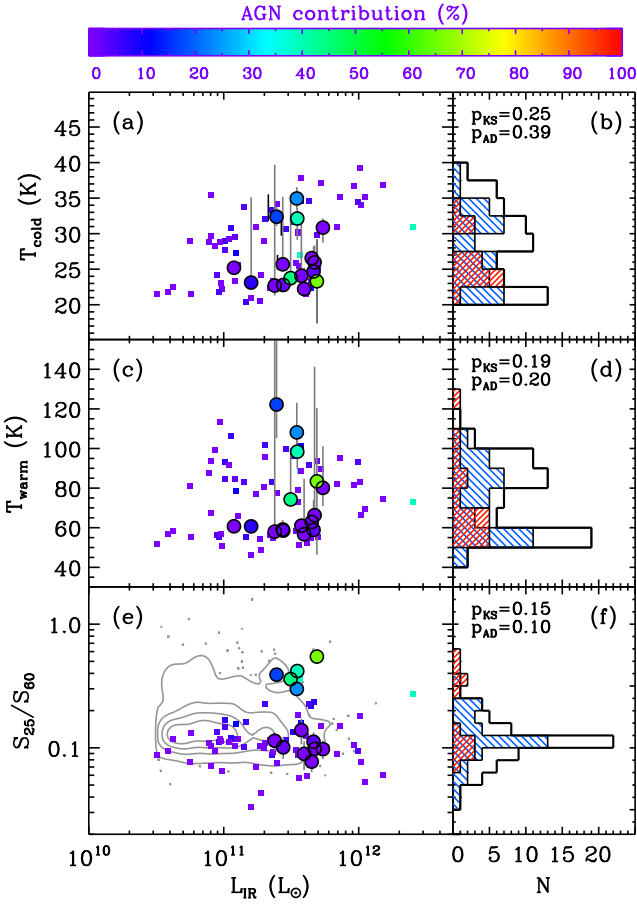


FIG. 3.— Dust temperature of the cold component for local DOGs (circles) and for other infrared luminous galaxies with submillimeter detection (squares) as a function of total infrared luminosity (a), and their histograms (b). Symbols are color-coded as shown by the color bar at the top to represent AGN contributions estimated from the SED decomposition. Error bars are plotted only for local DOGs for better visibility. The thick solid line histogram represents the distribution of all squares. The red (//) and blue (\) hatched histograms denote the local DOGs and the galaxies in the comparison sample in the same range of infrared luminosity $L_{\text{IR}}=1.19\text{--}5.43\times 10^{11}L_{\odot}$, respectively. Two numbers in the corner are p -values from the K-S and A-D k-sample tests between the two distributions. Same as (a–b), but for the dust temperature of the warm component (c–d) and for the flux density ratios between *IRAS* 25 and 60 μm (e–f). The gray dots and contours in panel (e) indicate the distribution of *IRAS*-detected SDSS galaxies at $z > 0.01$ regardless of submillimeter detection.

is also unaffected because of very small fraction of warm dust mass ($M_{\text{warm}}/M_{\text{dust}} \lesssim 1\%$).

Figures 3 and 4 show that the AGN-dominated DOGs (with $f_{\text{AGN}} > 10\%$) differ from the starburst-dominated DOGs (with $f_{\text{AGN}} \leq 10\%$) and from comparison galaxies even in the distributions of T_{cold} , M_{dust} , and $M_{\text{dust}}/M_{\text{star}}$ where we expect little AGN effects. Statistical tests for the three samples suggest that the difference in T_{cold} is insignificant, but is significant in M_{dust} and $M_{\text{dust}}/M_{\text{star}}$ (i.e., the dust masses of AGN-dominated DOGs are small). However, the limited numbers of AGN- and starburst-dominated DOGs in this study do not allow us to draw strong conclusions on the difference and its cause.

The bottom panels of Figure 4 show that the amount of warm dust in starburst-dominated local DOGs is three times larger than that in comparison galaxies; when we exclude the galaxies with $f_{\text{AGN}} > 10\%$, the me-

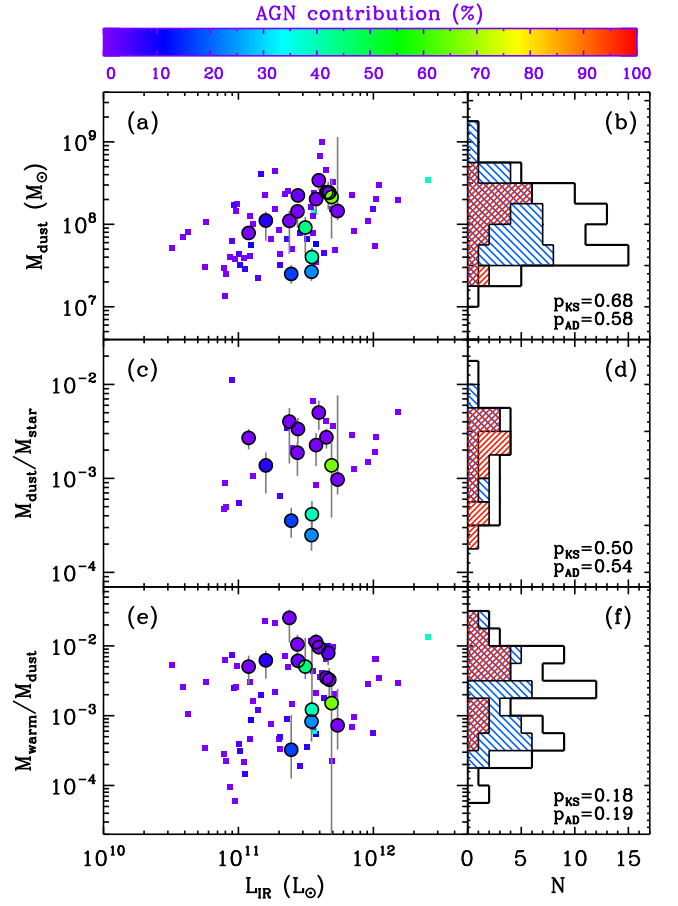


FIG. 4.— Same as Figure 3, but for the total dust mass (a–b), the dust-to-stellar mass ratio (c–d), and the dust mass fraction of warm component (e–f).

dian values of $M_{\text{warm}}/M_{\text{dust}}$ are 0.62% and 0.21% for local DOGs and comparison galaxies, respectively. Because the DOGs tend to be mid-infrared bright by definition, the large fraction of warm dust component in DOGs could be expected. However, the main reason for the extreme near-UV/mid-infrared flux density ratios of local DOGs is the abnormal faintness in the near-UV rather than the mid-infrared brightness (see Penner et al. 2012; HG13). It is thus not easy to understand why local DOGs have large warm dust fractions. Moreover, the warm dust fraction range of comparison galaxies is very broad (2.6 dex). Because we cannot rule out the possibility that the derived warm dust parameters are contaminated by the presence of (hidden) AGNs even in starburst-dominated DOGs, this finding needs to be confirmed with a method free from AGN contamination. Then, with a larger sample of DOGs, it is also necessary to examine what physical properties (e.g., stellar population, interstellar medium condition, extinction curve) are connected to this result.

On the other hand, the total dust masses of local DOGs are similar to those of other submillimeter-detected infrared luminous galaxies. Interestingly, the (cold) dust masses of hot DOGs at $z \gtrsim 2$ (i.e., extreme AGN-dominated DOGs) appear comparable to those of radio-detected quasars (Wu et al. 2014). Considering the large uncertainty in their dust mass estimates, Wu et al. suggest that the dust masses of hot DOGs could be also similar to those of submillimeter galaxies (SMGs). The

similar dust masses between DOGs and other galaxies at both low and high redshifts indicate that what makes DOGs special among dusty galaxies is not an overall amount of dust content. The other possible explanation for the extreme dust obscuration in local DOGs is that the dust distribution is spatially compact such as centrally concentrated and/or clumpy (strongly aligned with massive star-forming regions). To investigate the detailed dust distribution in local DOGs, we plan to observe the local DOGs with Atacama Large Millimeter Array (ALMA) and to look into the *Spitzer* archival images of very nearby DOGs. We are also studying the gas content of local DOGs from the James Clerk Maxwell Telescope (JCMT) observations, which can provide valuable information on their dust-to-gas ratios, star formation efficiency, and deviation from star-forming main sequence

(see [Daddi et al. 2010](#); [Elbaz et al. 2011](#)).

We thank the anonymous referee for his/her useful comments that improved the manuscript. We also thank Margaret Geller and Sean Andrews for helpful comments in early stages of this work. J.C.L. is a member of Dedicated Researchers for Extragalactic Astronomy (DREAM) in Korea Astronomy and Space Science Institute (KASI). G.H.L. acknowledges the support by the National Research Foundation of Korea (NRF) Grant funded by the Korean Government (NRF-2012-Fostering Core Leaders of the Future Basic Science Program). This material is based upon work at the Caltech Submillimeter Observatory, which is operated by the California Institute of Technology.

REFERENCES

- Abazajian, K. N., Adelman-McCarthy, J. K., Agüeros, M. A., et al. 2009, *ApJS*, 182, 543
- Armus, L., Mazzarella, J. M., Evans, A. S., et al. 2009, *PASP*, 121, 559
- Assef, R. J., Eisenhardt, R. P. M., Stern, D., et al. 2015, *ApJ*, 804, 27
- Assef, R. J., Kochanek, C. S., Brodwin, M., et al. 2010, *ApJ*, 713, 970
- Baldwin, J. A., Phillips, M. M., & Terlevich, R. 1981, *PASP*, 93, 5
- Behroozi, P. S., Wechsler, R. H., & Conroy, C. 2013, *ApJ*, 770, 57
- Berta, S., Lutz, D., Genzel, R., Förster-Schreiber, N. M., & Tacconi, L. J. 2016, *A&A*, 587, 73
- Berta, S., Lutz, D., Santini, P., et al. 2013, *A&A*, 551, 100
- Bian, F., Kewley, L. J., Dopita, M. A., & Juneau, S. 2016, *ApJ*, 822, 62
- Boselli, A., Ciesla, L., Cortese, L., et al. 2012, *A&A*, 540, 54
- Brand, K., Dey, A., Desai, V., et al. 2007, *ApJ*, 663, 204
- Bussmann, R. S., Dey, A., Borys, C., et al. 2009, *ApJ*, 705, 184
- Bussmann, R. S., Dey, A., Lotz, J., et al. 2011, *ApJ*, 733, 21
- Calanog, J. A., Wardlow, J., Fu, H., et al. 2013, *ApJ*, 775, 61
- Casey, C. M., Narayanan, D., & Cooray, A. 2014, *PhR*, 541, 45
- Charlot, S., & Fall, S. M. 2000, *ApJ*, 539, 718
- Ciesla, L., Boquien, M., Boselli, A., et al. 2014, *A&A*, 565, 128
- Ciesla, L., Charmandaris, V., Georgakakis, A., et al. 2015, *A&A*, 576, 10
- Clark, C. J. R., Dunne, L., Gomez, H. L., et al. 2015, *MNRAS*, 452, 397
- Clemens, M. S., Negrello, M., De Zotti, G., et al. 2013, *MNRAS*, 433, 695
- Cortese, L., Ciesla, L., Boselli, A., et al. 2012, *A&A*, 540, 52
- da Cunha, E., Charlot, S., & Elbaz, D. 2008, *MNRAS*, 388, 1595
- Daddi, E., Elbaz, D., Walter, F., et al. 2010, *ApJ*, 714, L118
- Dale, D. A., Aniano, G., Engelbracht, C. W., et al. 2012, *ApJ*, 745, 95
- de Grijp, M. H. K., Miley, G. K., Lub, J., & de Jong, T. 1985, *Nature*, 314, 240
- Desai, V., Soifer, B. T., Dey, A., et al. 2009, *ApJ*, 700, 1190
- Dey, A., Soifer, B. T., Desai, V., et al. 2008, *ApJ*, 677, 943
- Dickinson, M., Papovich, C., Ferguson, H. C., Budavári, T. 2003, *ApJ*, 587, 25
- Dowell, C. D., Allen, C. A., Babu, R. S., et al. 2003, *Proc. SPIE*, 4855, 73
- Draine, B. T. 2003, *ARA&A*, 41, 241
- Draine, B. T. & Lee, H. M. 1984, *ApJ*, 285, 89
- Draine, B. T., & Li, A. 2007, *ApJ*, 657, 810
- Dunne, L., Eales, S., Edmunds, M., et al. 2000, *MNRAS*, 315, 115
- Dunne, L., & Eales, S. A. 2001, *MNRAS*, 327, 697
- Elbaz, D., Dickinson, M., Hwang, H. S., et al. 2011, *A&A*, 533, 119
- Farrah, D., Lonsdale, C. J., Weedman, D. W., et al. 2008, *ApJ*, 677, 957
- Fiore, F., Grazian, A., Santini, P., et al. 2008, *ApJ*, 672, 94
- Greis, S. M. L., Stanway, E. R., Davies, L. J. M., & Levan, A. J. 2016, *MNRAS*, 459, 2591
- Hatziminaoglou, E., Omont, A., Stevens, J. A., et al. 2010, *A&A*, 518, L33
- Heckman, T. M., Hoopes, C. G., Seibert, M., et al. 2005, *ApJ*, 619, L35
- Hildebrand, R. H. 1983, *QJRAS*, 24, 267
- Houck, J. R., Soifer, B. T., Weedman, D., et al. 2005, *ApJ*, 622, L105
- Hwang, H. S., Andrews, S. M., & Geller, M. J. 2013, *ApJ*, 777, 38
- Hwang, H. S., & Geller, M. J. 2013, *ApJ*, 769, 116
- Hwang, H. S., Geller, M. J., Kurtz, M. J., Dell'Antonio, I. P., & Fabricant, D. G. 2012, *ApJ*, 758, 25
- Hwang, H. S., Elbaz, D., Dickinson, M., et al. 2011, *A&A*, 535, 60
- Hwang, H. S., Elbaz, D., Lee, J. C., Jeong, W. S., Park, C., Lee, M. G., & Lee, H. M. 2010a, *A&A*, 522, 33
- Hwang, H. S., Elbaz, D., Magdis, G., et al. 2010b, *MNRAS*, 409, 75
- James, A., Dunne, L., Eales, S., & Edmunds, M. G. 2002, *MNRAS*, 335, 753
- John, T. L. 1988, *A&A*, 193, 189
- Jones, S. F., Blain, A. W., Stern, D., et al. 2014, *MNRAS*, 443, 146
- Juneau, S., Bournaud, F., Charlot, S., et al. 2014, *ApJ*, 788, 88
- Kauffmann, G., Heckman, T. M., White, S. D. M., et al. 2003, *MNRAS*, 341, 33
- Kennicutt, R. C. 1988, *ARA&A*, 36, 189
- Kewley, L. J., Groves, B., Kauffmann, G., & Heckman, T. 2006, *MNRAS*, 372, 961
- Kirkpatrick, A., Pope, A., Sajina, A., et al. 2015, *ApJ*, 814, 9
- Kirkpatrick, A., Pope, A., Alexander, D. M., et al. 2012, *ApJ*, 759, 139
- Kovács, A. 2006, PhD thesis, Caltech
- Lee, J. C., Hwang, H. S., & Ko, J. 2013, *ApJ*, 774, 62
- Lee, J. C., Hwang, H. S., Lee, M. G., Kim, M., & Kim, S. C. 2011, *MNRAS*, 414, 702
- Lee, J. C., Hwang, H. S., Lee, M. G., Kim, M., & Lee, J. H. 2012, *ApJ*, 756, 95
- Leong, M., Peng, R., Houde, M., et al. 2006, *Proc. SPIE*, 6275, 21
- Madau, P., & Dickinson, M. 2014, *ARA&A*, 52, 415
- Magdis, G. E., Daddi, E., Béthermin, M., et al. 2012, *ApJ*, 760, 6
- Magdis, G. E., Elbaz, D., Hwang, H. S., et al. 2010, *MNRAS*, 409, 22
- Magdis, G. E., Rigopoulou, D., Helou, G., et al. 2013, *A&A*, 558, 136
- Magnelli, B., Popesso, P., Berta, S., et al. 2013, *A&A*, 553, A132
- Martin, D. C., Fanson, J., Schiminovich, D., et al. 2005, *ApJ*, 619, L1
- Melbourne, J., Peng, C. Y., Soifer, B. T., et al. 2011, *AJ*, 141, 141
- Mullaney, J. R., Alexander, D. M., Goulding, A. D., & Hickox, R. C. 2011, *MNRAS*, 414, 1082
- Murakami, H., Baba, H., Barthel, P., et al. 2007, *PASJ*, 59, 369
- Narayanan, D., Dey, A., Hayward, C. C., et al. 2010, *MNRAS*, 407, 1701
- Neugebauer, G., Habing, H. J., van Duinen, R., et al. 1984, *ApJ*, 278, L1
- Penner, K., Dickinson, M., Pope, A., et al. 2012, *ApJ*, 759, 28
- Rémy-Ruyer, A., Madden, S. C., Galliano, F., et al. 2013, *A&A*, 557, 95
- Rigby, E. E., Maddox, S. J., Dunne, L., et al. 2011, *MNRAS*, 415, 2336

- Riguccini, L., Le Floch, E., Ilbert, O., et al. 2011, *A&A*, 534, 81
Riguccini, L., Le Floch, E., Mullaney, J. R., et al. 2015, *MNRAS*, 452, 470
Sanders, D. B., & Mirabel, I. F. 1996, *ARA&A*, 34, 749
Sauvage, M., Tuffs, R. J., & Popescu, C. C. 2005, *Space Sci. Rev.*, 119, 313
Symeonidis, M., Vaccari, M., Berta, S., et al. 2013, *MNRAS*, 431, 2317
Toba, Y., & Nagao, T. 2016, *ApJ*, 820, 46
U, V., Sanders, D. B., Mazzarella, J. M., et al. 2012, *ApJS*, 203, 9
Veilleux, S., & Osterbrock, D. E. 1987, *ApJS*, 63, 295
Veilleux, S., Rupke, D. S. N., Kim, D., et al. 2009, *ApJS*, 182, 628
Vlahakis, C., Dunne, L., & Eales, S. 2005, *MNRAS*, 364, 1253
Walcher, J., Groves, B., Budavári, T., & Dale, D. 2011, *Ap&SS*, 331, 1
Willmer, C. N. A., Rieke, G. H., Le Floch, E., et al. 2009, *AJ*, 138, 146
Wilson, C. D., Petitpas, G. R., Iono, D., et al. 2008, *ApJS*, 178, 189
Wright, E. L., Eisenhardt, P. R. M., Mainzer, A. K., et al. 2010, *AJ*, 140, 1868
Wu, J., Busmann, R. S., Tsai, C.-W., et al. 2014, *ApJ*, 793, 8
Wu, J., Tsai, C.-W., Sayers, J., et al. 2012, *ApJ*, 756, 96
York, D. G., Adelman, J., Anderson, Jr., J. E., et al. 2000, *AJ*, 120, 1579